Chapter 2

Methods

This chapter presents a thorough overview of sample preparation details and the various characterization techniques employed in the studies. The samples were prepared using the arc melting technique. The characterization techniques involve laboratory and synchrotron x-ray diffraction for structural analysis, a scanning electron microscope coupled with an energy dispersive spectroscopy (EDS) detector for compositional analysis, and a Physical Properties Measurement System (PPMS) for magnetization measurements. The magnetotransport measurements were carried out using the Cryogen Free Measurement System (CFMS). The theoretical calculations were conducted using the Quantum Espresso software package within the scope of density functional theory (DFT). The Berry curvature-related properties were investigated using the Wannier90 package. The chapter delved into the principles and procedures of these experimental and theoretical methods.

2.1 Experimental method

2.1.1 Synthesis

The samples were synthesized using the standard arc melting technique, which is employed for melting metals, typically to synthesize alloys. The fundamental principle of the arc melting method involves heating via an electric arc formed between a Tungsten electrode and the metal piece kept in a copper hearth. This electric arc is generated by applying a large electric voltage to the Tungsten tip. The arc can reach temperatures of up to 3000 °C, sufficient for melting most metallic samples. The arc melting setup comprises three main components; vacuum unit, power source, and chiller. The vacuum unit, equipped with a rotary pump, can evacuate the chamber to as low as 10^{-3} mbar. The cooling, provided by the chiller, protects both the copper hearth and the Tungsten tip from melting during the high-temperature melting process. The power source is used to apply large electric tension at the tungsten tip. The high-pure (99.99%) of the raw elements and a Ti ball are kept inside two different crucibles of the copper hearth. Before the melting of the sample, the Ti ball is melted to form the TiO_2 layer on top of its surface if a trace amount of oxygen molecule is present inside the chamber. The alloy is melted cyclically, typically 4 to 5 times by flipping to ensure uniform mixing. After melting we measured the weight of the sample and below 1% of weight loss was noted for all the studied systems. The annealing of the samples was done in the

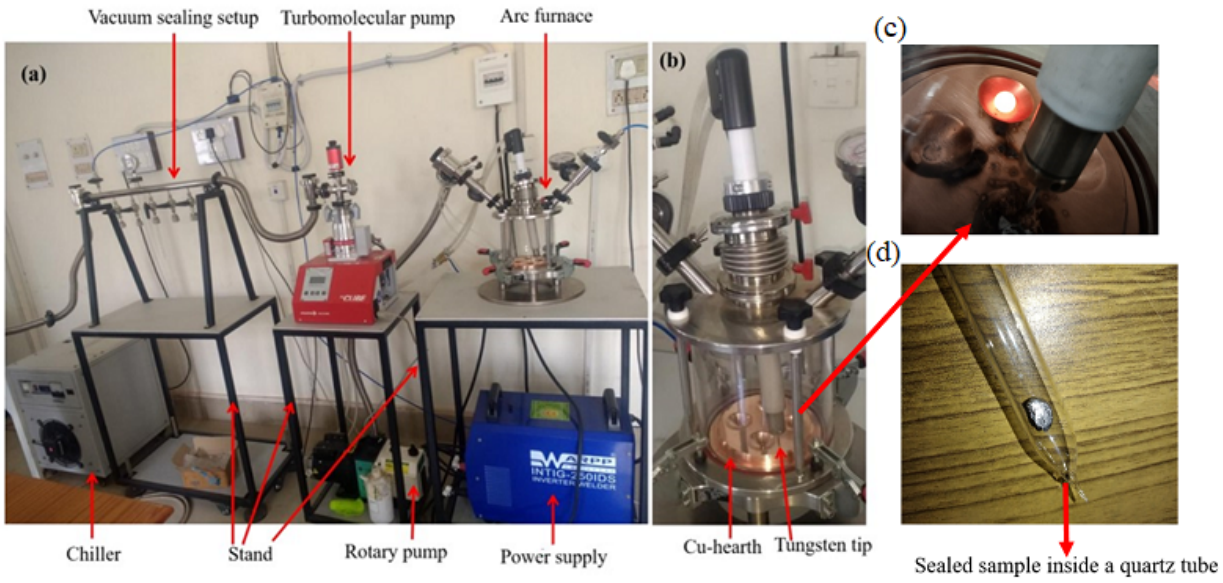

Figure 2.1: (a) An actual image of arc melting set-up. (b) Zoom view of the sample chamber. (c) An enlarged view of the copper hearth. (d) An image of a sample sealed inside the quartz tube.

box furnace capable of reaching a temperature as high as 1200 °C. The annealing process began with the sealing of the sample inside the evacuated quartz tube up to 10^{-6} mbar, using a diffusion pump. Subsequently, the quartz tube is kept inside the furnace for the annealing at the specified temperature and duration. An actual image of the arc melting set-up is shown in Fig. 2.1(a)-(c). Figure 2.1(d) shows an actual image of a sample sealed inside the quartz tube.

2.1.2 X-ray diffraction

The diffraction of X-rays from the material provides insights about the crystal structure. X-rays are electromagnetic waves of wavelength ranges from 0.1 Åto 100 Å, discovered in 1895 by W.C Rontgen [1]. Inspired by Ewald's Ph.D. dissertation on electromagnetic wave scattering by harmonic oscillators, von Laue proposed that a crystal composed of regularly spaced atoms could serve as an X-ray scattering center when the X-ray wavelength closely matches the interatomic spacing of the crystal. Friedrich and Knipping, guided by von Laue, provided the initial experimental confirmation of X-ray wave nature and the ordered atomic lattice within crystals by directing X-rays at copper sulfate, resulting in observable diffraction patterns on a photographic plate [2]. In 1914, Max von Laue received the Nobel Prize in Physics for his pioneering work on the diffraction of X-rays by crystals [3]. The account of this experiment was read by English physicist W.L Bragg,

who successfully analyzed the Lau diffraction pattern and proposed the necessary condition for the diffraction of X-rays from the crystal. Figure2.2 shows the crystal section exhibits parallel atomic

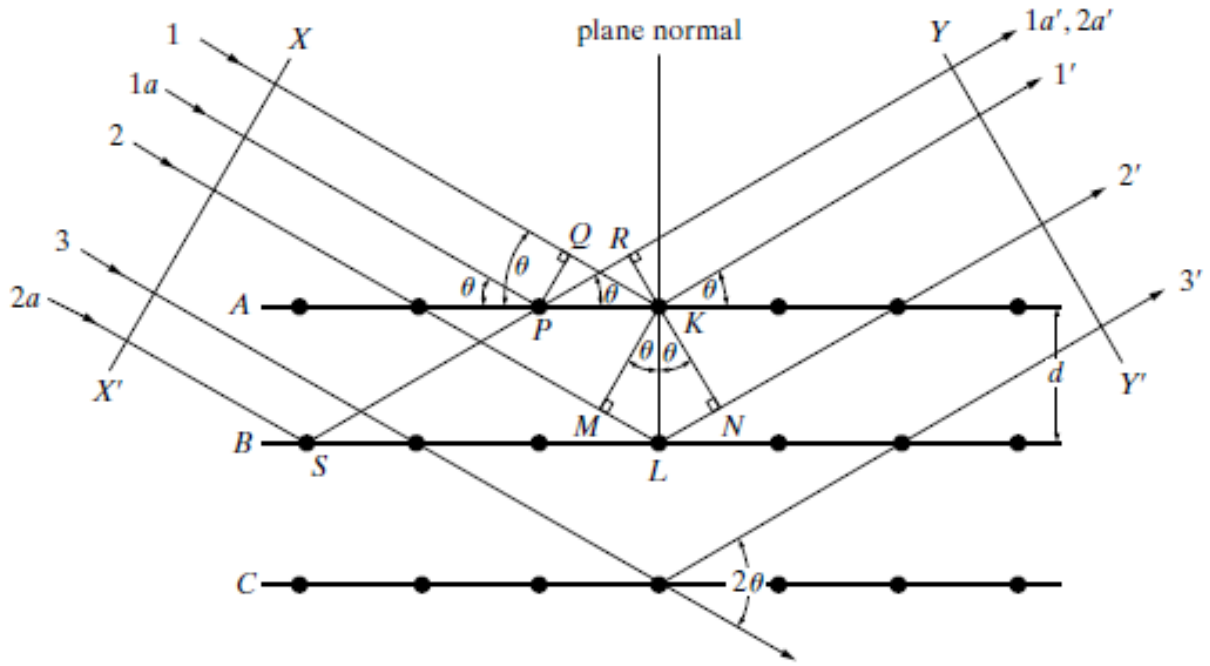

Figure 2.2: (a) X-ray diffraction from the crystal [2].

planes labeled A, B, and C each separated by a distance of d. Assume the set of parallel beams of X-ray is incident at angle θ with the atomic planes. The atoms scatter the X-rays in all directions, and in certain directions, the scattered X-ray beam will be in phase, reinforcing each other to form the diffracted beam. For example beams 1 and $1a$ incident at the atom K and P and diffracted in all directions. In most of the directions, the beams are out of phase but in some directions for example in 1' and $1a'$ the diffracted beams are in phase as the path difference QK-$PR = PK\cos\theta$ - $PK\cos\theta = 0$. This will be the same for all the individual planes but what will be the conditions for the reinforcement of scattered waves from different planes? The path difference of two waves 1 and 2 incident on the K and L point is the $ML + LN = 2d\sin\theta$. This will be the same for the overlapping X-rays S and P, as in this direction the path difference is zero between the S and L or P and K. Bragg suggested that the 1' and 2' will be in phase if the path difference is the integral multiple of the X-ray wavelength *i.e.*

$$2dsin\theta = n\lambda \tag{2.1}$$

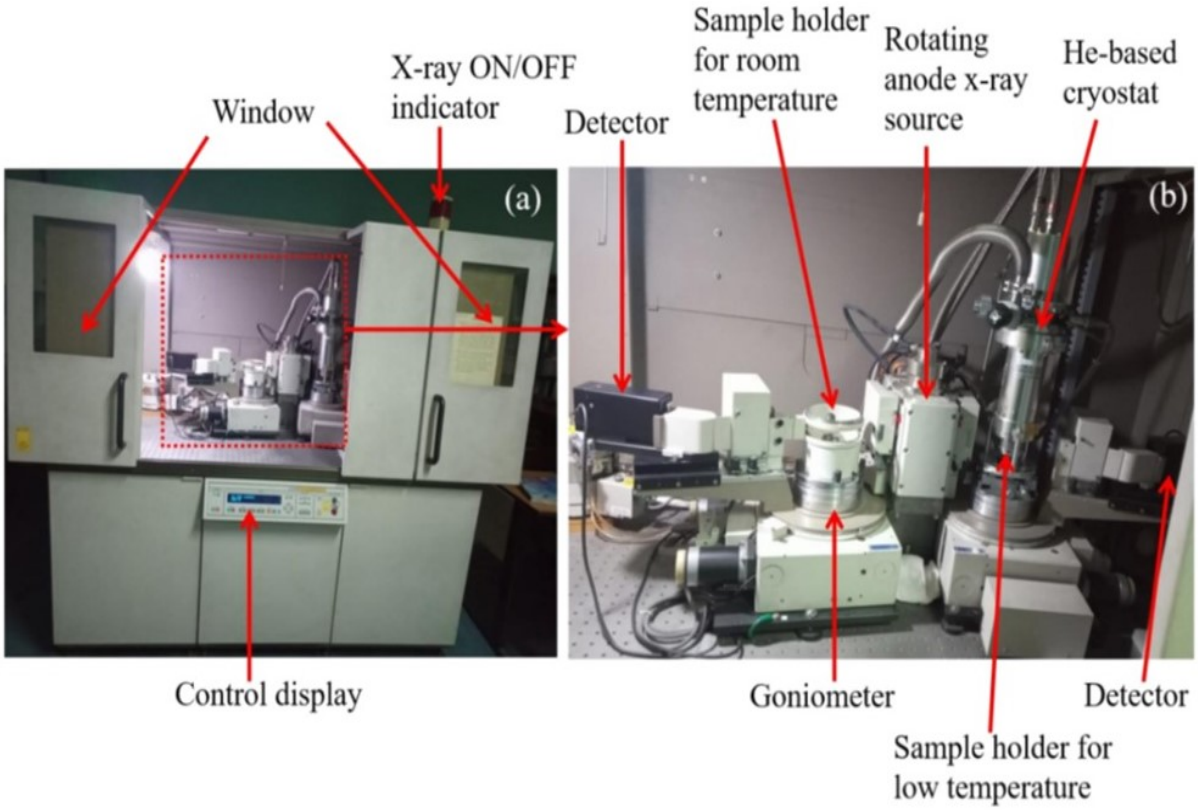

Figure 2.3: (a) An image of Rigaku X-ray diffractometer available in the School of Materials Science and Technology. (b) A close view of the diffractometer.

Eq.2.1 is known as Bragg's law. n is the order of diffraction. In the present study, the laboratory X-ray diffraction data was collected using an 18-kW Cu rotating anode-based high-resolution X-ray diffractometer fitted with a curved graphite crystal monochromator in the diffraction beam. This diffractometer works in the Bragg-Brentano geometry. An actual image of this diffractometer is given in Fig.2.3 (a) and (b), which is available in our lab.

2.1.3 Synchrotron X-ray diffraction

Synchrotron light is generated through the circular motion of electrons inside the tunnel when they decelerate by applying a magnetic field [4]. It is based on the principle of emission of radiation through the accelerated charge, e.g. when a moving electron changes its direction, it emits electromagnetic radiation or light. Synchrotron lights of different wavelengths are generated when electrons reach speeds sufficient (near the speed of light) to produce emitted light with wavelengths in the X-ray range on changing direction. Synchrotron-based X-ray sources offer numerous advan-

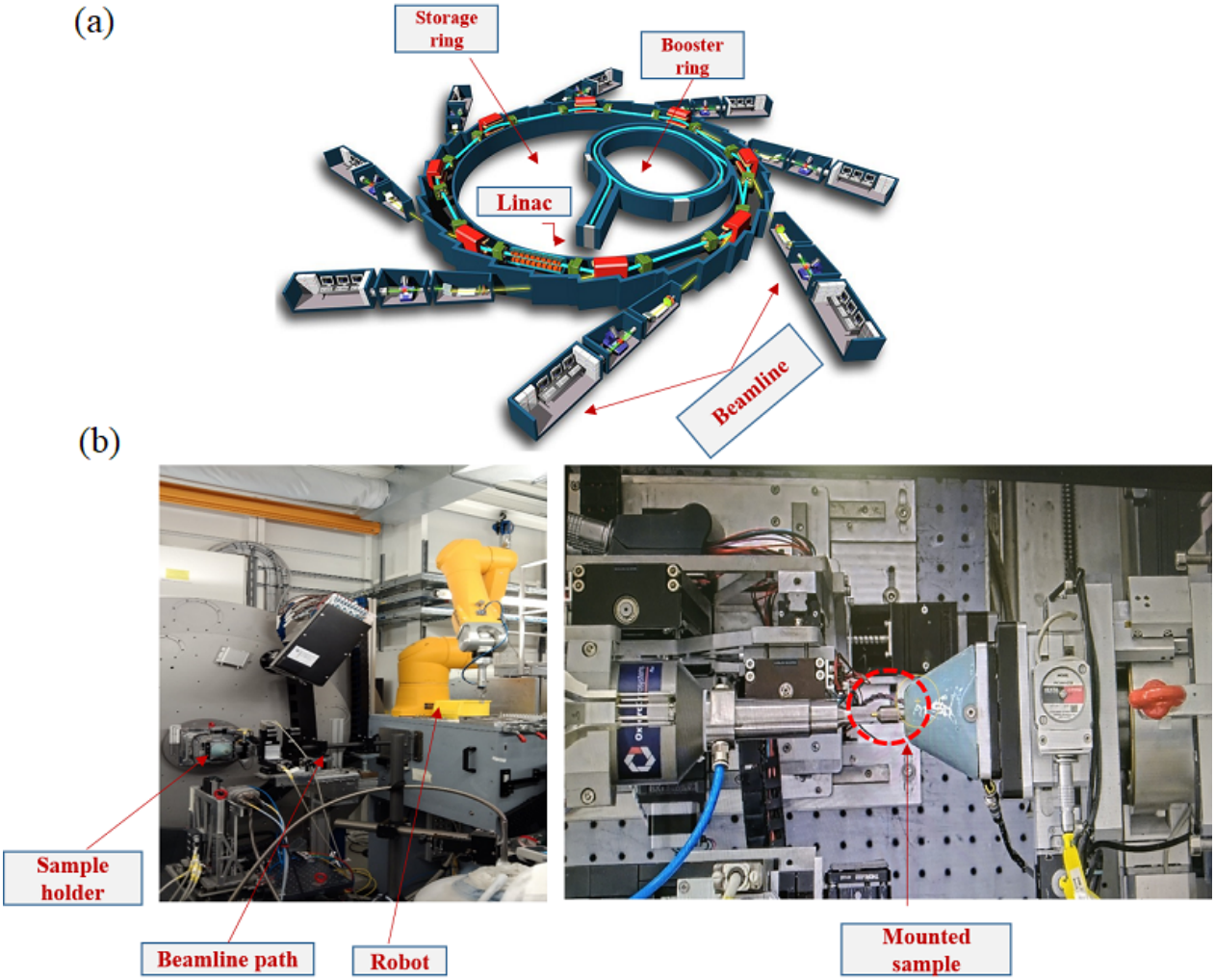

Figure 2.4: (a) A visual representation of the synchrotron light source and beamline [6]. (b) An actual image of the beamline station P2.01 at Petra III-DESY Germany.

tages over conventional laboratory-based X-ray sources, including high energy, heightened brilliance, a broader energy spectrum, wavelength adjustability, strong polarization, and ultra-short pulse emissions [4, 5]. Consequently, synchrotron X-ray enables the characterization of material structures with significantly greater detail compared to laboratory-based X-ray diffraction (XRD). There are different components involved in generating the synchrotron-based X-rays, as depicted by a schematic diagram in Fig.2.4 (a). These components are Linac, Booster ring, Storage ring, and Beamlines. The electrons are produced from the cathode say the tungsten tip by flowing current through it. The electron enters into the high vacuum tube and at the same time, the electrons are accelerated to high energy typically 250 million electron volts (MeV) using a Linear Accelerator (LINAC) in a straight line. At this energy, the electrons travel at 99.9998% of the speed of light. The electrons from Linac enter into the Booster ring where the radio frequency cavity further

increases the energy of electrons (GeV). The current electron energy levels are excessively high. Attempting to increase electron energy with common household batteries would necessitate connecting approximately 2 billion batteries in series. The booster ring transfers high-energy electrons to the storage ring, where they remain in circulation for periods ranging from 4 to 12 hours, generating light for the beamline. The storage ring is the series of magnets that produces the bending of the electrons, which causes the electrons to emit synchrotron light. The emitted light is guided to the experimental hutch through beamlines to characterize the materials. The beamlines contain a series of mirrors, monochromators, slits, and focusing devices to achieve the precisely required beam spot on the sample for the characterization. In the present study, the measurement was performed at PETRA-III DESY in Germany at the P2.01 beamline. An image of the experimental set-up at the P2.01 beamline is shown in Fig.2.4(b). The wavelength of the synchrotron X-ray produced at this beamline station is 0.20713 Å. For the synchrotron X-ray diffraction measurements, borosilicate capillaries were used as sample containers. The fine powder sample was packed in the borosilicate capillaries, spinning continuously during measurement to minimize the texturing effect in the synchrotron X-ray diffraction data. An actual image of the mounted capillary ready for diffraction measurement at the P02.1 beamline of PETRA-III is given inside the circle of the right panel in Fig.2.4(b). The high-resolution synchrotron X-ray diffraction data was collected by moving the 2D detector away from the sample about 1200-1500 mm.

2.1.4 Scanning electron microscope

Microscopy is the method of visualizing objects beyond the capabilities of the human eye. Optical microscopes use lenses to magnify objects, while electron microscopy relies on electrons instead of light for imaging [7]. In material science, electron microscopy is a vital tool for studying materials. The concept of electron microscopy is the de Broglie wavelength associated with the high energetic electron in the order of few Å/nm and hence this gives the resolution at the atomic level in the material [7].

The scanning electron microscope scans the surface of the material using a focused ion beam [9]. The primary electrons are generated by a source, a typical source is a tungsten filament. The primary electrons are guided toward the sample by the magnetic lenses. The interaction of the primary elec-

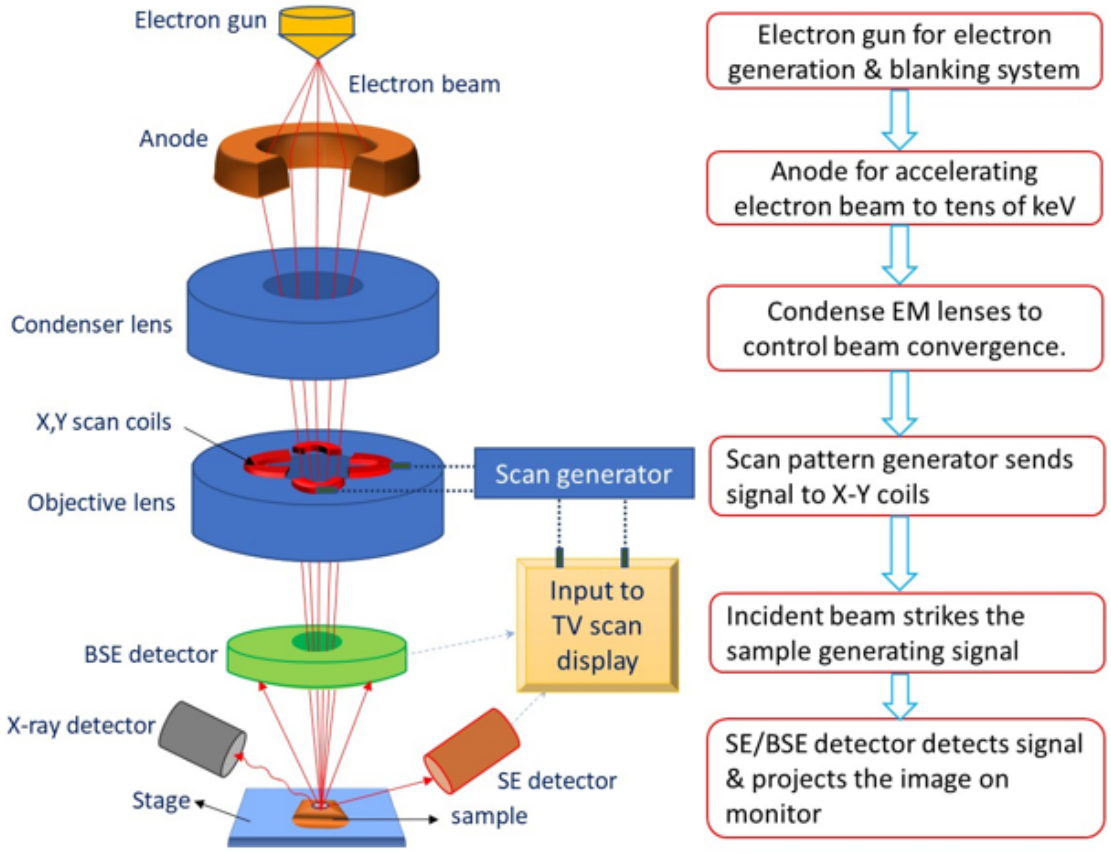

Figure 2.5: A schematic of scanning electron microscope [8].

trons with the sample leads to the generation of the backscattering electrons, secondary electrons, and characteristic X-rays [10]. Back-scattered electrons originate from a wide region within the sample volume, resulting from elastic interactions between electrons and atoms that alter the electron trajectories. The number of detected backscattered electrons correlates directly with the atomic number (Z), making backscattering imaging valuable for sample phase analysis [11]. Conversely, secondary electrons arise from inelastic collisions between incident electrons and the sample, primarily originating from the sample's surface or the near-surface regions [12]. Secondary electrons prove highly advantageous for inspecting the surface topography of the sample. The characteristic X-rays originate from the deceleration of the electron due to the repulsion from other electrons in the sample. Different detector is used to detect the different types of electrons. A schematic of a scanning electron microscope is shown in Fig. 2.5.

2.1.5 Magnetization measurements

The magnetization measurement of samples was conducted using the Physical Properties Measurement System (PPMS). This system utilizes a Vibrating Sample Magnetometer (VSM) to measure the magnetization of the materials [13]. The VSM, often referred to as the Foner magnetometer, is attributed to S. Foner [14]. The VSM operates on the principle of detecting changes in magnetic flux within a coil when a magnetized sample vibrates nearby [15]. A non-magnetic rod supports the sample at one end, while a linear motor is fixed to the other. As the sample oscillates, it generates an oscillating magnetic field, inducing an alternating electromotive force (emf) in the detection coil. The magnitude of this emf is directly proportional to the magnetic moment of the sample. The lock-in amplifier amplified the small emf to extract meaningful data. The VSM has a sensitivity of $<10^{-6}$ emu. Generally, the vibration frequency remains below 40 Hz, with a vibration amplitude typically measuring a few millimeters. In our investigation, we conducted magnetization

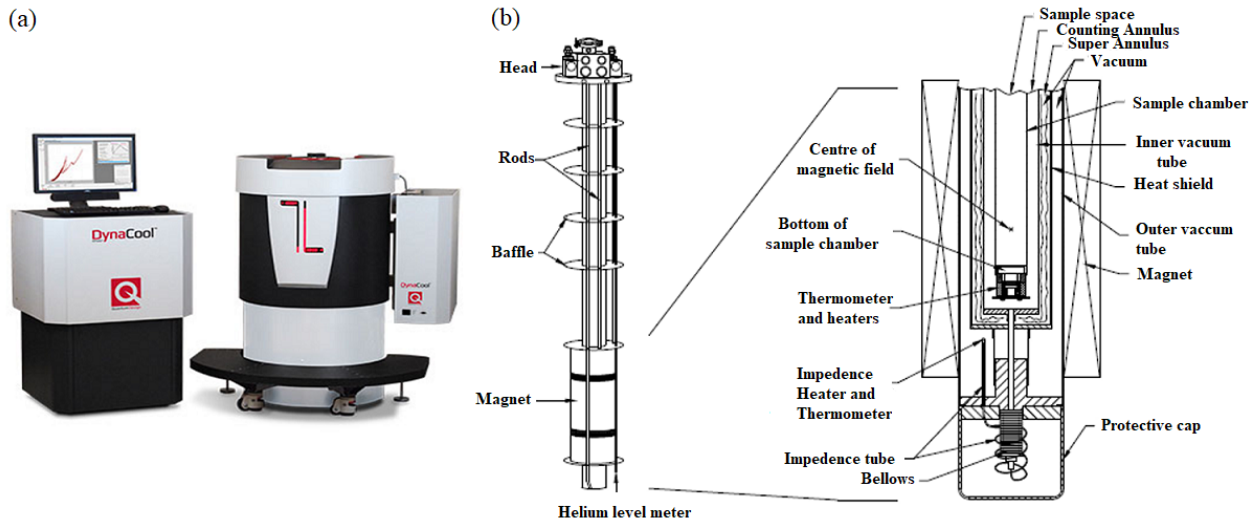

Figure 2.6: (a) An image of Physical Properties Measurement System (PPMS) of Quantum design. (b) The inner diagram of the PPMS instrument. [13, 15].

measurements across a temperature range of 2 K to 300 K, up to magnetic fields up to 5 T. Within the PPMS, the AC Measurement System (ACMS) option is available to perform ac-susceptibility $\chi(H)$ measurement. For $\chi(H)$ measurement, a small AC magnetic field is applied in addition to the DC field applied by a superconducting magnet and measures the sample magnetic moment response. The addition of an AC field makes the magnetization time-dependent leading to the change

in the magnetic flux in the pickup coil, and hence induces the voltage in the coil without necessitating any movement of the sample. The ac-susceptibility measurement gives both the amplitude and the phase. The amplitude is the change in the magnetic moment not the absolute magnetization. In our investigation, we measured the $\chi(H)$ in the field range of 2 K-300 K, up to a field of ± 1 T. Figure 2.6 (a) and (b) show the PPMS instrument from Quantum Design and a typical inner diagram of the instrument, respectively.

2.1.6 Transport measurements

The transport properties of the samples *i.e.* resistivity, magnetoresistance, and Hall measurements were conducted using the Cryogen Free Measurements System (CFMS) available in our lab. CFMS is a standard closed cycle refrigeration (CCR) based system and provides the variable temperature insert (VTI) in a range of 2 K-300 K and magnetic field of 7T using a superconducting solenoid magnet. The system is automated by Labview software. The rectangular-shaped sample was used

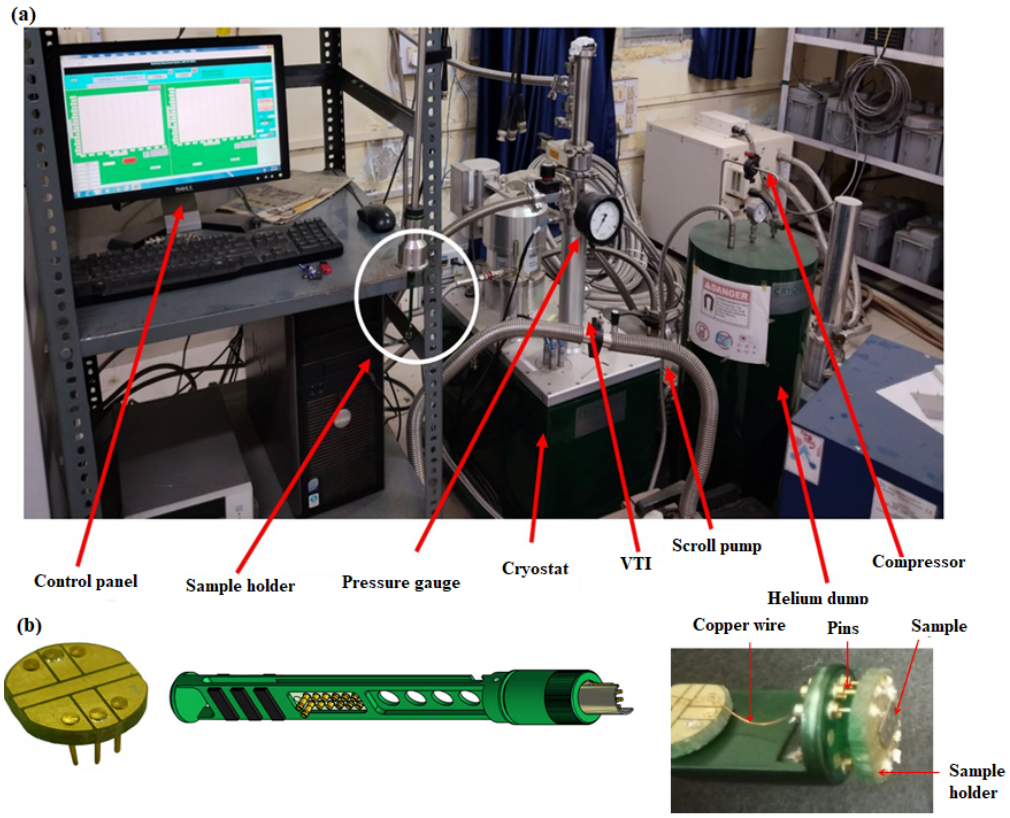

Figure 2.7: (a) An actual image of the cryogen-free measurement system (b) Sample holders and connections.

to conduct the transport measurements using the four-probe method. The current and voltage source

from the Keithley was used for providing the DC-current and measuring the voltage across the conductor. The sample is fixed on the sample holder using GE varnish. The contact on the sample was made by soldering the copper wires using the indium as a glue because of its low melting point (156 °C). A self-made connection between the sample and the current source as well as the nanovoltmeter was designed using the sample insert for the measurement. An actual image of the CFMS and the sample holder is shown in Fig. 2.7 (a) and (b), respectively.

2.2 Theoretical method

2.2.1 Density Functional Theory

The density functional theory (DFT) is the most popular method for the diverse modeling of materials in physics, chemistry, and material science, Walter Kohn (1923−2016) was awarded half of the 1998 Nobel Prize in chemistry for his pioneering work in advancing DFT [16–19]. DFT utilizes the Schrodinger equation to solve the Hamiltonian of the atomic system and gives the lowest energy configuration called the state of electrons. In quantum physics, the Schrödinger wave equation can be exactly solved for the hydrogen atom because it is a one-electron system with a simple Coulombic interaction between electrons and nuclei. Solving this equation reveals crucial information about the atom's behavior, such as its ground state energy and wave function, shedding light on its electronic structure and bonding properties [20, 21]. However, a system having more than two nuclei and electrons, makes the Hamiltonian more complex to solve analytically. Considering the system with a large number of atoms and electrons, it is not possible to solve the Schrodinger equation due to the complex Hamiltonian. Considering a system with n electrons and N nucleus, system's Hamiltonian can be expressed as [22]

$$\hat{H} = \frac{h^2}{2m}\sum_{i=1}^{n}\nabla_i^2 + \frac{h^2}{2M}\sum_{i=1}^{N}\nabla_i^2 + \sum_{i=1}^{n}\sum_{j=1,j\neq i}^{n}\frac{e^2}{|r_i - r_j|} + \sum_{i=1}^{n}\sum_{j=1}^{N}\frac{Ze^2}{|R_j - r_i|} + \sum_{i=1}^{N}\sum_{j=1j\neq i}^{N}\frac{Z_i Z_j e^2}{|R_i - R_j|} \quad (2.2)$$

and the Schrodinger's wave equation as,

$$\hat{H}\Psi\left(r_1, r_2, r_3, ..., r_n\right) = E\Psi\left(r_1, r_2, r_3, ..., r_n\right) \tag{2.3}$$

where *m* and *M* is mass of electron and Nucleus. The terms from left to right of the equation Eq.2.2 denote the kinetic energy of electrons, kinetic energy of the nucleus, Coloumb interaction between electrons, Coloumb interaction between the nucleus and electrons, and Coloumb interaction between the nucleus. Ψ is the wave function of all the *n* electrons whose spacial coordinates are given by the vectors $r_1, r_2, r_3, ..., r_n$. The solution space of the Schrodinger equation will *3n* dimensional as each electron can move in the three dimensions. In a real system where the atoms are in billion orders, solving the equation is quite challenging. This problem is known as a many-body problem in condensed matter physics. Therefore to solve the Schrodinger equation of many atoms in the system some approximations are needed. The first approximation is proposed by Max Born and J. Robert Oppenheimer which assumes the motion of electrons and nucleus separately. The nucleus, which is heavier than the electrons treated as stationary compared to the motion of electrons. Therefore the Hamiltonian of Eq.2.2 can be written as

$$\hat{H} = \frac{h^2}{2m}\sum_{i=1}^{n}\nabla_i^2 + \sum_{i=1}^{n}\sum_{j=1,j\neq i}^{n}\frac{e^2}{|r_i - r_j|} + \sum_{i=1}^{n}\sum_{j=1}^{N}\frac{Ze^2}{|R_j - r_i|} + \sum_{i=1}^{N}\sum_{j=1,j\neq i}^{N}\frac{Z_i Z_j e^2}{|R_i - R_j|} \tag{2.4}$$

Although this consideration, simplifies the equation but dimensionality of solution space does not reduce. It is worth mentioning that the wavefunction which is the function of a set of coordinates is not an observable quantity, it can be determined in terms of the probability distribution function given as [22];

$$n(r_1, r_2, r_3, ..., r_n) = \psi^*(r_1, r_2, r_3, ..., r_n)\psi(r_1, r_2, r_3, ..., r_n) \tag{2.5}$$

Here $n(r)$ represents an electronic charge density function, which describes the probability of finding electrons at r_i positions. This discussion highlights that electron density, represented as $n(r)$ with just three coordinates, holds a significant amount of observable information from the complete wave function solution to the Schrodinger equation, which deals with $3n$ coordinates. Therefore the goal is to find the system's electron density.

Hohenberg and Kohn-Sham Theorems

Hohenberg and Kohn-Sham proposed two theorems based on which the ground state energy of the system can be determined. The first theorem states that the *ground state energy from Schrodinger's wave equation is a unique functional of electron density of the system* [23].

$$E\left[n\left(r\right)\right] = E_{system} \tag{2.6}$$

The first theorem suggests that there is a direct one-to-one correspondence between the ground state wave function and electron density. Alternatively, the ground state electron density can uniquely determine the ground state wave function and energy. Now the problem is easy in the sense that the electron density with 3 variables can be used for solving the Schrodinger equation instead of the wave function with $3n$ variables. Although the first theorem does not say anything about the kind of functional. The second theorem describes the properties of functional and states that *electron density that minimizes the energy of the overall functional is the true electron density corresponding to the full solution of the Schrodinger equation* [22, 23]. If the 'accurate' functional is known then the electron density can be varied until the energy calculated from the known functional is minimized, which helps to find the right electron density. This variational principle is used for minimizing the energy with approximate forms of the functional. This energy functional can be expressed as [22]

$$E\left[n(r)\right] = E_{known}\left[n(r)\right] + E_{XC}\left[n(r)\right]$$

where,

$$E_{known}[n(r)] = \frac{h^2}{m}\sum_{i=1}^{n}\int \psi_i \nabla^2 \psi_i d^3r + \int V(r)n(r)d^3r + \frac{e^2}{2}\int\int \frac{n(r)n(r')}{|r-r'|}d^3r d^3r' + E_{ion-ion} \tag{2.7}$$

E_{known} comprises the kinetic energies of electrons, Coulombic interactions involving electrons and nuclei, interactions among electron pairs, and interactions among pairs of nuclei. On the other hand, E_{XC} represents the exchange-correlation term, including all quantum mechanical effects that

are absent in the "known" terms. Kohn-Sham demonstrated that determining the correct electron density can be reformulated as a problem of solving a set of equations, with each equation only involving a single electron [22].

$$\left[\frac{h^2}{2m}\nabla^2 + V(r) + V_H(r) + V_{XC}(r)\right]\psi_i(r) = E_i\psi_i(r) \tag{2.8}$$

This equation has the same form as the many-body problem, with the difference that it solves the single electron wave function which depends on just three spacial variables. The charge density solution for this hypothetical non-interacting system is considered to be the same as for the interacting system. The term *V(r)* defines the interaction between the collection of atomic nuclei and an electron. The term V_H is a Hartree term that defines the repulsion between the electron being considered in one Kohn-Sham equation and the total charge electron density defined by all electrons in the problem;

$$V_H(r) = e^2 \int \frac{n(r')}{|r - r'|} d^3r \tag{2.9}$$

$V_{XC}(r)$ defines the exchange and correlation potential, which include all the errors derived by the treatment of the non-interacting system apart from the classical Coloumb self-interaction term $V_H(r)$ [24, 25]. V_{XC} is defined as a functional derivative of the exchange-correlational energy,

$$V_{XC}(r) = \frac{\delta E_{XC}(r)}{\delta n(r)} \tag{2.10}$$

For solving the Kohn-Sham equation (Eq.2.8), we must define Hartee potential, however, defining the Hartree potential necessitates knowledge of the electron density. Calculating the electron density relies on knowing the single-electron wavefunction, and for this, we have to solve the Kohn-Sham equation. To break this circle, the iterative method should be considered in the following way which is known as self-consistence calculation (SCF) [22];

1. Specify an initial trial electron density.

2. Determine the single-electron wave function $\psi_i(r)$ by solving the Kohn-Sham equation.

3. Compute the electron density by $\psi_i(r)$ found from step 2, n_{ks}(r) = $2\sum_i \psi^*(r)\psi(r)$

4. Compare $n_{ks}(r)$ with the initial electron density, $n(r)$, used in solving the Kohn–Sham equations. If they match, it's the ground-state electron density, allowing total energy computation. If not, revise the trial electron density and repeat from step 2.

Exchange Correlational Functional

The exchange-correlation functional is a part of the total energy functional that describes the exchange and correlation effects of the electrons. The exchange term includes the antisymmetric nature of the electron wave function, reflecting the Pauli exclusion principle. The correlation term is the correlation effect between the electron beyond the classical Coloumb repulsion. Since we don't have exact information about the exchange-correlation potential, determining the ground state electron density of the many-body system is quite difficult. One idea for deriving an exchange-correlation function is based on the uniform electron gas *i.e.* $n(r)$=constant. The exchange-correlation potential can be defined as [22]

$$V_{XC}(r) = V_{XC}^{electrongas}[n(r)]. \tag{2.11}$$

The conceptual framework assumes electrons to be localized in the vicinity of positively charged nuclei. The approximation, in turn, is defined solely by the local density, leading to its classification as the local density approximation (LDA) [26]. The uniform electron gas is somewhat related to the metallic system, the LDA functional is good for the metallic system. However, in a more accurate perspective, the electron density exhibits a gradient, deviating from the strict homogenous gas model. Consequently, the exchange-correlation functional is influenced not only by the electron density but also by its associated gradient [26]. Therefore the best approximation after the LDA is the generalized gradient approximation (GGA) accounts for both the electron density $\rho(r)$ as well the gradient [26]. In calculations concerning solids, two of the most commonly applied functionals are the Perdew–Wang functional (PW91) and the Perdew–Burke–Ernzerhof functional (PBE) [24]. After choosing the exchange-correlation functional, the basis function is needed for the expansion of the wave function to model the electron density matrix. In context to study the electronic, magnetic, and transport properties of solids the plane wave basis is used to define the wave function. These plane wave basis functions are amplified with periodic functions as defined

by Bloch's theorem [27, 28]. This is needed to define the periodicity of the potential due to atoms.

2.2.2 Wannier interpolation

The electronic band structure of materials, as determined through DFT calculations, provides valuable insights into the relationship between energy and momentum for its electrons. However, this representation is quite abstract because it is based on plane waves that are delocalized throughout the entire material. In simpler terms, Wannier functions offer a means to represent this information in localized real space, known as the Wannier basis [29]. This localization is achieved by employing a Fourier transform on the Bloch wave function. The Fourier transformation of a plane wave is the Dirac delta function centered at the origin of the wave. This transformation effectively localizes the wave function. The Wannier functions are particularly useful because they provide a clear picture of how electrons are distributed in real space within the crystal lattice [29]. Due to the localization, it can be used to perform computationally expensive high-quality interpolations of the band struc-

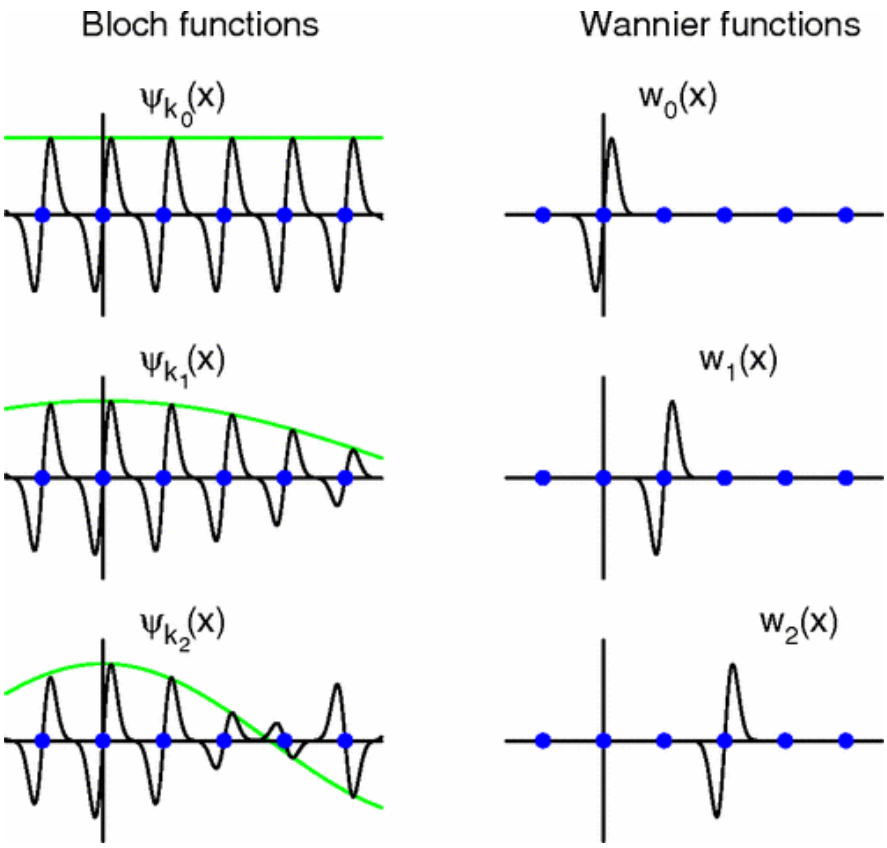

Figure 2.8: (a) Transformation of Bloch wave function to Wannier functions. Solid circles represent lattice vectors, while thin lines represent the envelopes of each Bloch function, characterized by e^{ikx} [30].

ture, which is necessary to compute many physical quantities such as the Seebeck coefficient, Berry curvature-related properties, etc. which are very expensive to calculate in the plane wave basis [29]. In the periodic lattice, one-particle effective Hamiltonian $\hat{H}$, commutes with the translation vector $\hat{T_R}$, which allows to choice of the common eigenstate (ψ_{nk}-one particle orbital) according to the Bloch theorem

$$[\hat{H}, \hat{T_R}] = 0 \rightarrow \psi_{nk}(r) = u_{nk}(r)e^{-ikr}$$

The left column of Fig.2.8 shows the Bloch wave function, where at the center of the Brillouin zone (Γ-point) the eigenstates vary periodically as the lattice periodicity. At the off-center point in the Brillouin zone, the plane wave is modulated by periodic potential and decays with distances. It is clear that the eigenstates in the momentum space are delocalized [30]. The idea is to take these wave functions $\psi_{nk}(r)$ and make a unitary transformation in real space localized form. Gregory Wannier introduced a formula for these transformed states, known as Wannier functions, which can be expressed as [30]

$$|R_n\rangle = \int_{BZ} \psi_{nk}(r)e^{-ik\cdot R}dk \tag{2.12}$$

$$\Psi_{nk} = \sum_R e^{ik\cdot R}|R_n\rangle \tag{2.13}$$

where R is the Bravice lattice vector. Therefore any Bloch function can be built by superposition of the Wannier function if appropriate $e^{ik\cdot R}$ is used. The Bloch wave function and Wannier functions are related to the unitary transformation, therefore both result in equally valid descriptions, even if the Wannier functions are not eigenstate of the Hamiltonian. The concept of Wannier function quickly adapted in solid state physics but the practical implementation lags behind several years. A major reason for this is that Wannier functions are strongly nonunique [29] because of the phase indeterminacy of Bloch orbitals ψ_{nk} at every point nk e.g. if ψ_{nk} is the good eigenstate of the Schrodinger equation then ψ_{nk} multiplied by any phase factor can also be a good solution of Schrodinger equation. Therefore for the different gauges, the shape and spread of function will be different. Given the invariance of traces over this band manifold to unitary transformations among the J Bloch orbitals at a specific wave vector, it's logical to extend the concept of a gauge transformation to [30]

$$|\tilde{\Psi}_{nk}\rangle = \sum_{m=1}^{j} U_{mn}^{(k)}|\psi_{mk}\rangle \tag{2.14}$$

Here $U_{mn}^{(k)}$ is the Unitary transformation of dimension J. Defining the projection operator

$$P = \sum_{n=1}^{J} |\psi_{nk}\rangle\langle\psi_{nk}| = \sum_{n=1}^{J} |\tilde{\psi}_{nk}\rangle\langle\tilde{\psi}_{nk}|$$

The projection operator remains invariant even though the $|\tilde{\Psi}_{nk}\rangle$ is not an eigenstate of H. It should be noted that the wave function $\psi_{nk}(r)$ must be smooth for the well-localized gauge transformation. Therefore Unitary matrix must be chosen in such a way that it cancels out the discontinuities and stores the smooth wave function $|\tilde{\psi}_{nk\rangle}$. Therefore the Wannier Function can be written as [30]

$$|R_n\rangle = \int_{BZ} e^{-ik\cdot R} dk \sum_{n=1}^{J} U_{mn}^{(k)} |\psi_{mk}\rangle \tag{2.15}$$

It is always convenient to work in discrete k points rather than the continuous space. if N is the number of unit cells in the supercell, then Eq.2.12 can be written as [30]

$$|R_n\rangle = \frac{1}{\sqrt{N}} \sum_{k} \psi_{nk}(r) e^{-ik\cdot R} dk \tag{2.16}$$

One question arises here how to choose the unitary rotation matrix $U_{mn}^{(k)}$ to get the well-localized real space Wannier function. Let us define a localization functional [29–31]

$$\Omega = \sum_{n} [\langle 0n|r^2|0n\rangle - \langle 0n|r|0n\rangle^2] = \sum_{n} [\langle r^2\rangle - \bar{r_n}^2] \tag{2.17}$$

which evaluates the collective quadratic dispersion of the Wannier functions within the home unit cell, relative to their centers. The subsequent stage involves representing Ω using the Bloch wave function. However, this task needs more care as the position operator does not yield well-defined expectation values within the Bloch formalism. The maximally localized Wannier functions are obtained by minimizing the spread defined in Eq.2.17, concerning the unitary transformation matrix $U_{mn}^{(k)}$ [30]. This is performed by first calculating the Bloch orbital wave function ψ_{nk} using the self-consistence calculation in the framework of DFT. The $U_{mn}^{(k)}$ undergoes iterative refinement via a direct minimization process of the localization functional.

Now we discuss the procedure and requirement of Wannier interpolation. The Wannier interpola-

tion is a technique, that ranges from the simple band calculation to the calculation of various physical quantities in the Brillouin zone [32, 33]. These physical quantities often require the fine sampling of the Brillouin zone for convergence [30]. This is often the case in the metal, where the Fermi surface exhibits sharp discontinuities in k-space. Figure 2.9 represents the procedure of Wannier interpolation. The first principle calculations are usually carried out on a uniform coarse grid (left panel), and the physical interest quantity $f(q)$ is extracted from the Bloch eigenstate. The states within the chosen band are subsequently converted into Wannier functions, thereby transforming $f(q)$ into $f(R)$ in the Wannier formalism (middle panel). Due to the spatial localization of the Wannier functions, $f(R)$ decays rapidly with R. Now, by performing an inverse transformation, $f(R)$ can be accurately interpolated at any arbitrary k point in reciprocal space (right panel). This method effectively captures variations in $f(k)$ across reciprocal lengths finer than those defined by the first-principles mesh spacing. The Wannier functions are very useful for calculating the prop-

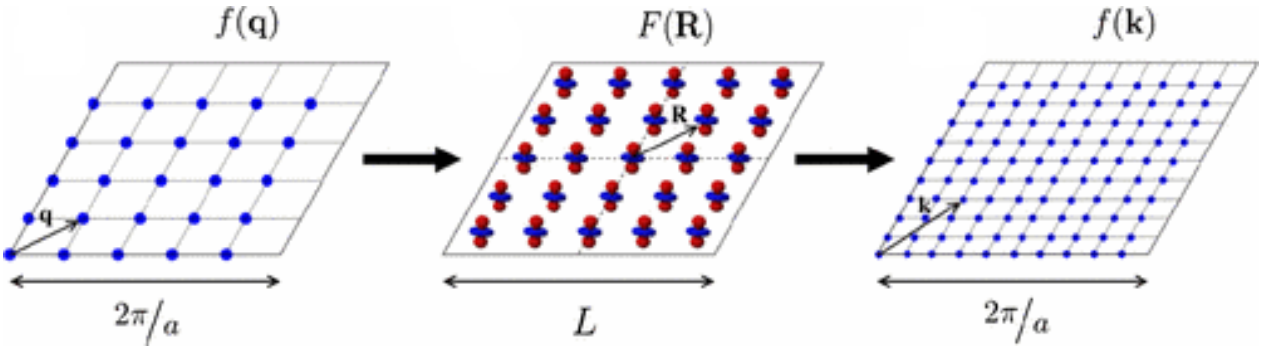

Figure 2.9: (a) Schematic view of the Wannier interpolation process [30].

erties related to the k-space derivative like Berry curvature [32]. Since in the metal, the k-space Berry curvature shows a strong and rapid variation, therefore the ultradense k-mesh is needed for the convergence of calculation [30]. This kind of situation is where the use of the Wannier function is more beneficial. The Wannier interpolation method is also useful for the calculation of orbital magnetization, optical properties, electron-phonon coupling, etc [29, 30, 34]. We have used the Wannier90 package for the Wannier interpolation and the calculation of Berry curvature and the intrinsic anomalous Hall conductivity (AHC). WannierTool software was used for the calculation of the topological properties of Materials. The intrinsic AHC was calculated using the Kubo formula [35]

$$\sigma_{\alpha\beta} = -\frac{e^2}{\hbar}\sum_n \int \frac{d^3k}{(2\pi)^3}\Omega^n_{\alpha\beta} f_n \tag{2.18}$$

where Berry curvature Ω can be written as a sum over eigenstate

$$\Omega^n_{\alpha\beta} = i \sum_{n \neq n'} \frac{\langle n|\frac{\partial H}{\partial k^\alpha}|n'\rangle\langle n'|\frac{\partial H}{\partial k^\beta}|n\rangle - (\alpha \leftrightarrow \beta)}{(\epsilon_n - \epsilon'_n)^2} \tag{2.19}$$

where, $|n\rangle$ represents an energy eigenstate of Hamiltonian H, with ϵ_n denoting its corresponding eigenvalue. The function f_n denotes the Fermi distribution function. The sign of AHE is influenced by the distribution of the Berry curvature and the sign of the effective spin-orbit coupling parameter [36, 37]. The change in the electronic band structure via doping, applying external pressure, spin reorientation, or varying the material's thickness, etc can result in the redistribution of the Berry curvature and consequently alter the AHE sign. For example, in CeAlSi, changing the magnetic field from the c-axis to the a-axis alters the AHE sign by modifying the Berry curvature [36]. Similarly, in Mn_3Ge the application of pressure above 1.53 GPa changes the sign of AHE [38]. The change in the sign of AHE is reported in 5 QL V-doped Sb_2Te_3 due to the reconstruction of Berry curvature on increasing the thickness of top topological insulator layer [39]. According to equation Eq.2.18, the sign of anomalous Hall conductivity (AHC) is opposite to the sign of the Berry curvature; a negative Berry curvature results in a positive AHC, and vice versa. When the internal magnetization is in the

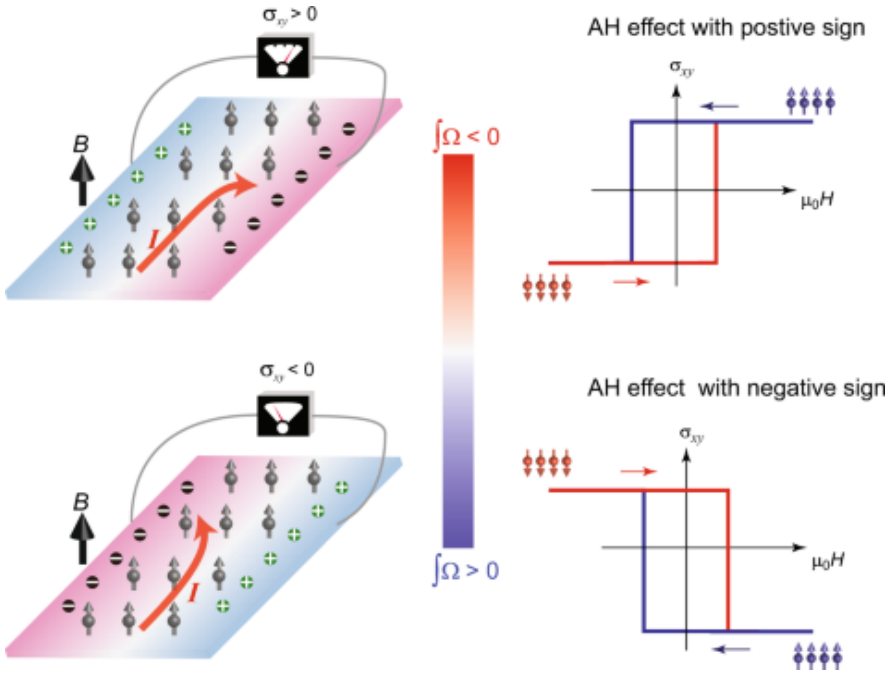

Figure 2.10: (a) An illustration of the relationship between the sign of AHC and Berry curvature [39].

upward direction, the electrons move to the higher potential side for negative Berry curvature and

hence the AHC is positive. When the Berry curvature is positive the electrons move to the lower potential side under positive internal magnetization and therefore AHC becomes negative [39]. This relationship between the sign of Berry curvature and AHC is shown in Fig.2.10. A sign change of AHE can occur due to the change in the sign of the effective spin-orbit coupling parameter, when the Fermi energy crosses the overlapping band upon doping of foreign element [37]. It is worthwhile to mention that reversing the polarity of the voltage lead changes the sign of Hall voltage. However, this change in sign is due to the configuration of the measurement setup and not the intrinsic AHE itself. This is a consequence of the measurement method applicable to any voltage measurement, not just for AHE. For a specific polarity configuration, the intrinsic sign of the AHE is determined by the sign of the Berry curvature and the effective spin-orbit coupling parameter [36, 37].

The AHC comes from the Berry curvature of all occupied bands, while the anomalous Nernst conductivity (ANC) stem from both occupied and unoccupied bands but near the Fermi level, therefore temperature role is obvious in context to ANC [40]. The anomalous Nernst conductivity (ANC) at temperature T can be evaluated as

$$\alpha_{ij}^{A}(T,\mu) = -\frac{1}{T}\frac{e}{\hbar}\sum_{n}\int \frac{d^3k}{(2\pi)^3}\Omega_{ij}^{n}[(E_n-\mu)f_n + K_BT\,ln(1+exp(-\frac{E_n-\mu}{K_BT}))]. \quad (2.20)$$

Near zero temperature, the above equation can be written as

$$\frac{\alpha_{ij}^{A}}{T} = -\frac{\pi^2}{3}\frac{k_B^2}{e}\frac{d\sigma_{\mathrm{ij}}}{d\mu} \quad (2.21)$$

where α_{ij}^{A}, k_B, σ_{ij} and μ are the ANC, Boltzmann constant, AHC, and chemical potential, respectively.

2.2.3 Micromagnetic simulation: A tool for simulation of skyrmions

Micromagnetic simulation is a framework for the study of magnetic dynamics of the system in a length scale greater than the interatomic distances [41]. Using micromagnetic simulation one can predict the equilibrium spin structure of the system utilizing the minimizing of the magnetization

energy. The micromagnetic theory involves the Brown and Landau-Lifshitz-Gilbert equation (LLG) equations. Brown's equation provides the criterion for minimizing the total magnetic energy [41]

$$\boldsymbol{M} \times \boldsymbol{H_{eff}} = 0$$

Here, the $\boldsymbol{M}$ is magnetization and $\boldsymbol{H_{eff}}$ is the total effective field. For typical magnetic materials, the $\boldsymbol{H_{eff}}$ can be given as

$$\boldsymbol{H_{eff}} = \boldsymbol{H_{ext}} + \boldsymbol{H_{exc}} + \boldsymbol{H_{dem}} + \boldsymbol{H_{anis}}$$

Here $\boldsymbol{H_{ext}}$, $\boldsymbol{H_{exc}}$, $\boldsymbol{H_{dem}}$, and $\boldsymbol{H_{anis}}$ represent the external magnetic field, the exchange field, the demagnetizing field, and the anisotropy field, respectively. Other field terms such as DMI or magnetostriction can be added if applicable to the system. In order to describe the precession of $\boldsymbol{M}$ about $\boldsymbol{H_{eff}}$, Landau and Lifshitz suggested [42];

$$\frac{d\boldsymbol{M}}{dt} = -\gamma(\boldsymbol{M} \times \boldsymbol{H_{eff}}) \tag{2.22}$$

where γ is the gyromagnetic ratio. Equation 2.22 is known as the Landau-Lifshitz equation. To account for the phenomenological damping, Gilbert modified Eq. 2.22 by introducing a damping term [43]

$$\frac{d\boldsymbol{M}}{dt} = -\gamma(\boldsymbol{M} \times \boldsymbol{H_{eff}}) - \frac{\alpha\gamma}{M_s}\boldsymbol{M} \times (\boldsymbol{M} \times \boldsymbol{H_{eff}}) \tag{2.23}$$

Equation 2.23 is known as Landau- Lifshitz-Gilbert equation (LLG) equation. The bold color represents vectorial quantities. The LLG equation describes the precession of magnetic moment M in a solid and is generally used in micromagnetics to model the effect of the magnetic field in ferromagnetic materials. For example, the micromagnetic simulation is widely used for the investigation of skyrmions in the magnetic systems [44–46].

References

[1] EC Watson. The discovery of x-rays. *Am. J. Phys.*, 13(5):281–291, 1945.

[2] Bernard Dennis Cullity. *Elements of X-ray Diffraction*. Addison-Wesley Publishing, 1956.

[3] Timir Datta. Laue: right or wrong? *Phys. Scr.*, 90(3):038002, 2015.

[4] Setsuro Ebashi, M Koch, and Edward Rubenstein. Handbook on synchrotron radiation. 1991.

[5] I Munro and G Marr. Synchrotron radiation sources. *Handbook on Synchrotron Radiation*, 2, 2013.

[6] S Kaiser Ali, Umashankar Das, Yanjie Lu, Vijayanada Kundapur, and Tim May. Synchrotron radiation: Applications in diagnosis and treatment of malignant brain tumors. In *Diagnostic techniques and surgical management of brain tumors*. IntechOpen, 2011.

[7] Ernst Ruska. The development of the electron microscope and of electron microscopy. *Rev. Mod. Phys.*, 59(3):627, 1987.

[8] Basics of scanning electron microscopy: Secondary electron and BSE imaging mode. URL https://emb-iitk.vlabs.ac.in/exp/sem-basics/theory.html.

[9] KCA Smith and CW Oatley. The scanning electron microscope and its fields of application. *Br. J. Appl. Phys.*, 6(11):391, 1955.

[10] Karen D Vernon-Parry. Scanning electron microscopy: an introduction. *III-Vs review*, 13(4): 40–44, 2000.

[11] JA Venables and CJ Harland. Electron back-scattering patterns—a new technique for obtaining crystallographic information in the scanning electron microscope. *Philosophical Magazine*, 27(5):1193–1200, 1973.

[12] Hellmut Seiler. Secondary electron emission in the scanning electron microscope. *J. Appl. Phys.*, 54(11):R1–R18, 1983.

[13] I Quantum Design. Vibrating sample magnetometer (VSM) option userâ azs manual. *California, United States: Author*, 2011.

[14] Simon Foner. Vibrating sample magnetometer. *Rev. Sci. Instrum.*, 27(7):548–548, 1956.

[15] Bernard Dennis Cullity and Chad D Graham. *Introduction to magnetic materials*. John Wiley & Sons, 2011.

[16] Eberhard Engel. *Density functional theory*. Springer, 2011.

[17] Wolfram Koch and Max C Holthausen. *A chemist's guide to density functional theory*. John Wiley & Sons, 2015.

[18] Paul Geerlings, Frank De Proft, and Wilfried Langenaeker. Conceptual density functional theory. *Chem. Rev.*, 103(5):1793–1874, 2003.

[19] Kieron Burke. Perspective on density functional theory. *J. Chem. Phys.*, 136(15):150901, 2012.

[20] Larry K Haines and David H Roberts. One-dimensional hydrogen atom. *Am. J. Phys.*, 37(11): 1145–1154, 1969.

[21] DGW Parfitt and ME Portnoi. The two-dimensional hydrogen atom revisited. *J. Math. Phys.*, 43(10):4681–4691, 2002.

[22] David S Sholl and Janice A Steckel. *Density functional theory: a practical introduction*. John Wiley & Sons, 2022.

[23] Viraht Sahni and Viraht Sahni. The hohenberg-kohn theorems and kohn-sham density functional theory. *Quantal Density Functional Theory*, pages 99–123, 2004.

[24] Matthias Ernzerhof and Gustavo E Scuseria. Assessment of the perdew–burke–ernzerhof exchange-correlation functional. *J. Chem. Phys.*, 110(11):5029–5036, 1999.

[25] Troy Van Voorhis and Gustavo E Scuseria. A novel form for the exchange-correlation energy functional. *J. Chem. Phys.*, 109(2):400–410, 1998.

[26] Paul Ziesche, Stefan Kurth, and John P Perdew. Density functionals from lda to gga. *Comput. Mater. Sci.*, 11(2):122–127, 1998.

[27] Charles Kittel. *Introduction to solid state physics*. John Wiley & sons, inc, 2005.

[28] Neil W Ashcroft and N David Mermin. *Solid state physics*. Cengage Learning, 2022.

[29] Nicola Marzari, Ivo Souza, and David Vanderbilt. An introduction to maximally-localized Wannier functions. *Psi-K newsletter*, 57:129, 2003.

[30] Nicola Marzari, Arash A Mostofi, Jonathan R Yates, Ivo Souza, and David Vanderbilt. Maximally localized wannier functions: Theory and applications. *Rev. Mod. Phys.*, 84(4):1419, 2012.

[31] Ivo Souza, Nicola Marzari, and David Vanderbilt. Maximally localized Wannier functions for entangled energy bands. *Phys. Rev. B.*, 65(3):035109, 2001.

[32] Xinjie Wang, Jonathan R Yates, Ivo Souza, and David Vanderbilt. Ab initio calculation of the anomalous Hall conductivity by Wannier interpolation. *Phys. Rev. B.*, 74(19):195118, 2006.

[33] Jonathan R Yates, Xinjie Wang, David Vanderbilt, and Ivo Souza. Spectral and fermi surface properties from Wannier interpolation. *Phys. Rev. B.*, 75(19):195121, 2007.

[34] Stepan S Tsirkin. High performance Wannier interpolation of Berry curvature and related quantities with WannierBerri code. *Npj Comput. Mater.*, 7(1):33, 2021.

[35] M Gradhand, DV Fedorov, Falko Pientka, P Zahn, I Mertig, and BL Györffy. First-principle calculations of the Berry curvature of Bloch states for charge and spin transport of electrons. *J. Condens. Matter Phys.*, 24(21):213202, 2012.

[36] Md Shahin Alam, Amar Fakhredine, Mujeeb Ahmad, PK Tanwar, Hung-Yu Yang, Fazel Tafti, Giuseppe Cuono, Rajibul Islam, Bahadur Singh, Artem Lynnyk, et al. Sign change of anomalous Hall effect and anomalous Nernst effect in the Weyl semimetal CeAlSi. *Phys. Rev. B*, 107(8):085102, 2023.

[37] Wei-Li Lee, Satoshi Watauchi, VL Miller, RJ Cava, and NP Ong. Dissipationless anomalous Hall current in the ferromagnetic spinel $CuCr_2Se_{4-x}Br_x$. *Science*, 303(5664):1647–1649, 2004.

[38] RD dos Reis, M Ghorbani Zavareh, MO Ajeesh, LO Kutelak, AS Sukhanov, Sanjay Singh,

J Noky, Y Sun, JE Fischer, K Manna, et al. Pressure tuning of the anomalous Hall effect in the chiral antiferromagnet Mn_3Ge. *Phys. Rev. Mater.*, 4(5):051401, 2020.

[39] Fei Wang, Xuepeng Wang, Yi-Fan Zhao, Di Xiao, Ling-Jie Zhou, Wei Liu, Zhidong Zhang, Weiwei Zhao, Moses HW Chan, Nitin Samarth, et al. Interface-induced sign reversal of the anomalous Hall effect in magnetic topological insulator heterostructures. *Nat. commun.*, 12 (1):79, 2021.

[40] Jonathan Noky, Johannes Gooth, Claudia Felser, and Yan Sun. Characterization of topological band structures away from the fermi level by the anomalous Nernst effect. *Phys. Rev. B.*, 98 (24):241106, 2018.

[41] D Kumar and AO Adeyeye. Techniques in micromagnetic simulation and analysis. *J. Phys. D: Appl. Phys.*, 50(34):343001, 2017.

[42] Charles H Stapper Jr. Micromagnetic solutions for ferromagnetic spheres. *J. Appl. Phys.*, 40 (2):798–802, 1969.

[43] Thomas L Gilbert. A phenomenological theory of damping in ferromagnetic materials. *IEEE Trans. Magn.*, 40(6):3443–3449, 2004.

[44] Subir Sen, Charanpreet Singh, Prashanta K Mukharjee, Ramesh Nath, and Ajaya K Nayak. Observation of the topological Hall effect and signature of room-temperature antiskyrmions in Mn-Ni-Ga D_{2d} Heusler magnets. *Phys. Rev. B.*, 99(13):134404, 2019.

[45] Giovanni Finocchio and Buttner et al. Magnetic skyrmions: from fundamental to applications. *J. Phys. D: Appl. Phys.*, 49(42):423001, 2016.

[46] Dola Chakrabartty, Sk Jamaluddin, Subhendu K Manna, and Ajaya K Nayak. Tunable room temperature magnetic skyrmions in centrosymmetric kagome magnet Mn_4Ga_2Sn. *Commun. Phys.*, 5(1):189, 2022.